



Efficiently unbiased solar-to-ammonia conversion by photoelectrochemical Cu/C/Si-TiO₂ tandems

Jingjing Ding ^a, Yanhong Lyu ^a, Huaijuan Zhou ^b, Bernt Johannessen ^c, Xiaoran Zhang ^a, Jianyun Zheng ^{a,*}, San Ping Jiang ^d, Shuangyin Wang ^a

^a State Key Laboratory of Chem/Bio-Sensing and Chemometrics, College of Chemistry and Chemical Engineering, Hunan University, Changsha, PR China

^b Advanced Research Institute of Multidisciplinary Sciences, Beijing Institute of Technology, Beijing 100081, China

^c Australian Synchrotron, Clayton, Victoria 3168, Australia

^d Foshan Xianhu Laboratory of the Advanced Energy Science and Technology Guangdong Laboratory, Foshan 528216, China



ARTICLE INFO

Keywords:

Solar-to-ammonia conversion
Photoelectrochemical nitrate reduction reaction
Bias-free cell
Hierarchical-structured Si-based photocathode

ABSTRACT

Photoelectrochemical nitrate reduction reaction (PEC NO₃RR) is of interest as a promising route to directly realizing the solar-to-ammonia (NH₃) conversion but the limited efficiency and high applied bias voltage hamper its commercial prospects. Here, we report a bias-free photoelectrochemical cell for PEC NO₃RR in aqueous conditions, achieving a substantial NH₃ yield rate of 13.1 μmol·h⁻¹·cm⁻², high faradaic efficiency of 93.8%, and recorded solar-to-NH₃ conversion of ~1.5% under 1 sun illumination. A hierarchical-structured Si-based photocathode with Cu⁺/Cu²⁺-containing Cu nanoparticles cocatalysts achieves a highly efficient PEC NO₃RR with NH₃ yield rate of 115.3 μmol·h⁻¹·cm⁻² in a three-electrode system. Integrating operando characterizations and systematic PEC measurements, the formation of Lewis acid sites on Cu nanoparticles by accepting the photoinduced electrons is the dominant factor for facilitating the absorption and hydrogenation of nitrate. This work will guide the development of a robust, high-performance, and unbiased PEC device for sustainable solar-to-NH₃/other fuels conversion.

1. Introduction

Ammonia (NH₃) is one of the most significant commodity chemicals and is currently consumed in the fertilizer, pharmacy and chemical industry [1–3]. In addition, NH₃ has recently attracted more attention as a carbon-free energy carrier for worldwide transportation of renewable energy (e.g. hydrogen) [4,5]. In 2022, the annual production of NH₃ exceeded 150 million tons [6], and with the breakthrough for the application in the energy field, the demand for NH₃ will greatly exceed the present annual value in the foreseeable future [7]. Nitrate (NO₃⁻) is the highest oxidation state of nitrogen, which is usually produced by the combustion and oxidation of NH₃ [8]. Significant qualities of NO₃⁻ can be accumulated in the human living environment, leading to serious environmental pollution problems [9]. Therefore, developing green and sustainable technologies to convert excess NO₃⁻ species into NH₃ is desired, which can facilitate the artificial nitrogen cycle and maintain global nitrogen balance.

In comparison to nitrogen gas (N₂) as the feedstocks, NO₃⁻ with a lower dissociation energy (204 kJ·mol⁻¹ for N = O) and higher solubility

in aqueous solution is more easily reduced to NH₃ [10,11]. In recent years, significant effort has been devoted to advance the prospects of synthesizing NH₃ from electrochemical NO₃⁻ reduction reaction (NO₃RR) [12]. Wang *et al.* [13] first proposed electrochemical NO₃RR as a potential green route for NH₃ production by platinum foil cathode. Not only noble metal (e.g. Pd, Ru and Au) [14–18] but also cheap transition metal (e.g. Fe, Ni and Cu) [19–23] as electrocatalysts have showed outstanding electrochemical NO₃RR performance. Recently, a high NH₃ yield rate of 875 ± 232 μg·h⁻¹·cm⁻² and good faradaic efficiency (FE) of ~65% at –0.6 V versus reversible hydrogen electrode (vs. RHE) have been obtained on a Cu-organic molecular solid electrocatalyst by electrocatalytic NO₃RR [24]. In addition, Fe single-atom catalysts deposited on a glassy carbon electrode have also shown an impressive NH₃ yield rate of ~20 mg·h⁻¹·mg_{cat}⁻¹ at –0.85 V vs. RHE [25]. Although some good achievements on NH₃ yield rate and FE have been reported [26,27], the electrocatalytic NO₃RR process still requires high applied voltages to synthesize NH₃ production in most cases, leading to high consumption of electric energy [12,28].

Utilizing solar energy to directly generate NH₃ via NO₃RR with zero

* Corresponding author.

E-mail address: jyzheng@hnu.edu.cn (J. Zheng).

bias is an innovative and exciting route for meeting the requirements of green synthesis[29]. In this regard, photoelectrochemical (PEC) device by combining the catalyst and the solar absorbers can be considered as an effective and viable solution to realize the high-performance and bias-free NO_3RR because of the compensation of photovoltage [30]. However, in the current research work, the special applied bias is still used in the PEC system to drive the NO_3RR . For example, Kim et al. have demonstrated that the Au-decorated ordered silicon nanowires (SiNWs) as photocathode presented an excellent FE of 95.6% with a low NH_3 yield rate ($\sim 4 \mu\text{g}\cdot\text{h}^{-1}\cdot\text{cm}^{-2}$) at 0.2 V vs. RHE in a three-electrode system [31]. In fact, the NH_3 yield rate is at low levels between 0.01 and 10 $\mu\text{g}\cdot\text{h}^{-1}\cdot\text{cm}^{-2}$ that it is difficult to firmly attribute it to PEC NO_3RR and exclude the disturbance of contaminations owing to NH_3 that may be present in air ($\sim 0.1 \text{ ppm}$), human breath ($\sim 0.3 \text{ ppm}$) and ion-conducting membranes, leading to a “false-positive” result [32,33]. Furthermore, a NH_3 yield rate of $\sim 8.2 \mu\text{g}\cdot\text{h}^{-1}\cdot\text{cm}^{-2}$ and FE over 80% at $\sim 0.2 \text{ V}$ vs. RHE for PEC NO_3RR have been acquired on the defect-engineered TiO_x cocatalyst/ $\text{CdS}/\text{Cu}_2\text{ZnSnS}_4$ photocathode [34]. Therefore, an unbiased PEC device for NO_3RR with high efficiency and rates is still a challenge for scientific foundation and commercial prospects.

Herein, we showcase a high-performance and unbiased PEC device combining the Si-based photocathode with the bulk TiO_2 photoanode on the same plane for NO_3RR . On this occasion, an acceptable NH_3 yield rate of $13.1 \mu\text{mol}\cdot\text{h}^{-1}\cdot\text{cm}^{-2}$ with an excellent FE of 93.8% and recorded solar-to-ammonia (STA) conversion of $\sim 1.5\%$ is reached under solar irradiance without applied bias. In addition, we also emphasize the benefits of this emerging concept using Cu^+ -containing Cu nanoparticles (NPs) as cocatalysts on the C-decorated nano-tapered n^+ -p-Si photocathode. The systematic operando analyses reveal new insights into the catalytic mechanism of NO_3RR by photogenerated Lewis acid sites of Cu NPs. To this end, we introduce a tandem photocathode-photoanode configuration as a promising alternative to conventional single photocathodes, enabling an extension of the PEC scope to NO_3 -to- NH_3 conversion.

2. Experimental methods

2.1. Material synthesis

2.1.1. Silicon wafer pretreatment

First, we prepared n^+ -p-Si. p-type silicon wafer was immersed in 80 $^\circ\text{C}$ 2% potassium hydroxide aqueous solution and maintained for 1-hour etching. After that, the etched silicon wafer was immersed in 5% HF solution for 3 min, then washed with deionized water and dried up in cold air. 0.1419 g P_2O_5 was ultrasonically dissolved in 10 mL absolute alcohol. 1–2 drops of 0.1 mol/L P_2O_5 solution were dropped on the etched surface of the silicon wafer with an area of about 2 cm^2 , followed by a high-temperature penetration at 800 $^\circ\text{C}$ for 8 min in a vacuum rapid annealing furnace. Finally, the sample was taken out from the furnace and washed in 5% HF solution for 1 min.

2.1.2. Photocathode assembly

To prepare the photocathode, 2 mg carbon material (900 $^\circ\text{C}$ carbonization of 5-Aminouracil) was dissolved in the mixture of 950 μL isopropanol and 50 μL Naffion, the resultant solution was coated on the surface of n^+ -p-Si with a load of $50 \mu\text{L}/\text{cm}^2$ and dried up under infrared light. Finally, the CSi sample was obtained. The prepared CSi was fixed on the carrier plate of the magnetron sputtering system. The deposition vacuum level is $3.0 \times 10^{-4} \text{ Pa}$. Copper target with a diameter of 60 mm and thickness of 4 mm was utilized. The substrate was cleaned under an 8.6 Pa Argon (Ar) atmosphere for 10 min. During the copper deposition process, a direct-current (DC) power of 15 W was applied, and the working pressure kept at 1 Pa. After deposition for 7 min, the thin film material CuCSi was formed. Later, the prepared CuCSi was annealed at 800 $^\circ\text{C}$ for 2 min. The backside of the silicon wafer was deposited with

Au thin film under a DC power of 10 W for 5 min by using an Au target. Finally, the CuCSi-800 sample was obtained. In addition, CuCSi sample was annealed at 200 $^\circ\text{C}$, 400 $^\circ\text{C}$, 600 $^\circ\text{C}$. Correspondingly, the samples were labeled as CuCSi-200, CuCSi-400, and CuCSi-600. The CuC-800 samples in EC tests were assembled in the same way as CuCSi-800 except for replacing the n^+ -p-Si substrate with carbon paper. The optimal size of the copper strip was pasted on the Au side of CuCSi-800 by silver glue and dried up under a vacuum of 40 $^\circ\text{C}$ for 2 h. The epoxy was used to encapsulate the edge and back of the silicon wafer and copper strip immersed by the electrolyte, then dried up in the air for 2 h.

2.1.3. Photoanode assembly

Single-sided polished p-type silicon wafers with an orientation of (100) were selected as substrates and cleaned in ethanol for 20 min. The clean and dry Si wafers were loaded into the deposition chamber. The sputtering chamber was vacuumed in advance to reach a vacuum degree of $3.0 \times 10^{-4} \text{ Pa}$. The substrate was cleaned under an 8.6 Pa Ar atmosphere for 10 min. For the deposition of a thin layer of titanium (Ti), the pressure in the sputtering chamber was maintained at 2 Pa and the deposition was carried out by using a direct-current power of 430 W for 5 min. The narrow edge of the Ti layer was left out and covered with a small silicon wafer to avoid the deposition of the subsequent material. After the deposition of the titanium thin film, oxygen (O_2) was added to the Ar atmosphere with an O_2/Ar ratio of 1:1, and the total pressure was maintained at 2 Pa. Subsequently titanium oxides (TiO_2) thin film was formed after sputtering for 4 h. The optimal size of a copper strip was pasted on the leave-out narrow edge mentioned above with silver glue and dried up at room temperature for 10 h. The epoxy was used to encapsulate the edge and back of the silicon wafer and copper strip immersed by the electrolyte, then dried up in the air for 2 h to get the final TiO_2 photoanode.

2.1.4. PEC device assembly

One quartz glass with an area of $3 \times 4 \text{ cm}^2$ was selected as the substrate. The surface of the quartz glass with the area of $1.5 \times 1.5 \text{ cm}^2$ blank was covered with silica gel for installing CuCSi-800, and the rest area was firstly deposited with titanium (2 Pa, 430 W, 5 min, Ar, 39.7 sccm). Subsequently, the titanium-covered surface was deposited with TiO_2 (2 Pa, 430 W, 5 min, Ar/ O_2 , 20/20 sccm) except for two conductive contact points covered with small silicon wafers. Then, all the small silicon wafers and silica gel on the quartz glass were taken down and the copper tape was pasted with silver glue, followed by adhering $1 \times 1 \text{ cm}^2$ CuCSi-800 to the copper strip in the blank area of the quartz glass. Finally, epoxy is used as described above.

2.2. Characterization

The morphologies of photoelectrodes were characterized by scanning electron microscopy (SEM) using a SU 8220 field emission scanning electron microscope. High-resolution field emission transmission electron microscopy (TEM) images and elemental mapping analysis were performed on a SU 8220 field emission transmission electron microscopy. X-ray diffraction (XRD) was measured by Bruke D8 Discover with the radiation of $\text{Cu K}\alpha$ in the 20 range from 30 to 60 degrees and the scan rate is 1 $^\circ/\text{min}$. The X-ray absorption spectra (XAS) on Cu for different annealing and reaction samples were recorded by the XAS Beamline (12ID) at the Australian Synchrotron in Melbourne, the test samples for XAS were assembled on carbon papers by replacing the silicon substrates with carbon papers and the other processes were same as the CuCSi-800 (see the details of photocathode assembly below). With the beamline optics employed (Si-coated collimating mirror and Rh-coated focusing mirror) the harmonic content of the incident X-ray beam was negligible. Inductively coupled plasma optical emission spectrometry (ICP-OES) was carried out on the Agilent 5110 (America) to quantify the copper ions in the electrolyte after reactions. The elements and valence states were conducted by X-ray photoelectron spectroscopy (XPS) operating on

ESCALAB Xi+ (Thermo Fisher Scientific, USA). Fourier transform infrared spectroscopy (FTIR) was carried out on the Thermo Scientific Nicolet iS5, Spotlight 400/400 N. Raman spectra were obtained by using a Witec Raman microscopy system (Alpha 300 R) with a laser wavelength of 532 nm and 100 \times magnification objective. For the measurement, the applied laser power, integration time, and accumulation were 0.5 mW, 5 s, and 9 times, respectively. NMR dates were obtained on a 600 MHz NMR instrument (Bruker) and EIS tests were conducted on Autolab PGSTAT302N (Eco Chemie, Utrecht, Netherlands). DRS was performed on a UV-visible-near-IR spectrophotometer (Hitachi, UV-4100).

2.3. Photoelectrochemical measurements

The CuCSi-800 photocathode photoelectrochemical performance was evaluated in an H-type cell with three electrodes under simulated 1 Sun illumination (100 mW/cm², AM 1.5 G), and pretreated Nafion 117 membrane served as the separator. The electrolytes in the cathode chamber contained 1 M KOH and 50 mM KNO₃. The photocathode is a silicon wafer sample with an area of about 0.5 \times 0.5 cm². The counter electrode is a platinum tablet while Ag/AgCl (saturated KCl solution) serves as the reference electrode and is converted to the RHE reference scale using $E_{RHE} = E_{Ag/AgCl} + 0.059 \times pH + 0.197$. The pH value is 13.8. The Ar gas is constantly purged in the electrolyte from one side of the cathode chamber and then exits from the other side to collect the ammonia product gas insoluble in the electrolyte. LSVs were conducted at a scan rate of 20 mV s⁻¹ with chopped light alternating between dark and light every 3 s. The TiO₂ photoanode photoelectrochemical performance was also tested under the same condition.

PEC measurement for the two-electrode device was carried out in a single cell with a flat quartz glass window under simulated 1 Sun illumination (100 mW/cm², AM 1.5 G) and the electrolyte consisted of 50 mM KNO₃ and 1 M KOH. The exposed copper strip is above the liquid level, and the front face of the device was immersed in the electrolyte perpendicular to the direction of incident light.

2.4. Detection of products

The ammonia product was quantified by the indophenol blue method with the three chromogenic agents: a, 1 M NaOH solution containing 5 wt% sodium citrate and 5 wt% salicylic acid; b, 0.05 M sodium hypochlorite solution; c, 1 wt% sodium nitroferricyanide solution. 0.9 mL of the electrolyte was extracted and 1 mL of a, 0.5 mL of b and 0.1 mL of c were added into the electrolyte in turn, then the mixture was kept in dark for 2 h before measurement of the absorbance. The absorbance at 662 nm by ultraviolet-visible (UV-Vis) spectrophotometer exhibits a linear relationship with the concentration of ammonia. The standard curve of indophenol blue method for the quantification of ammonia is shown in Fig. S13. Equations for NH₃ yield rate and Faradaic efficiency:

$$NH_3 \text{ yield rate } \left(\mu\text{mol h}^{-1} \text{ cm}^{-2} \right) = \frac{C_{NH_3} \times V}{t \times A}$$

$$NH_3 \text{ faradaic efficiency} = \frac{n \times F \times C_{NH_3} \times V}{M \times Q} \times 100\%$$

where C_{NH₃} (μg mL⁻¹) is the concentration of the product, V (mL) represents the volume of the reaction electrolyte (6.5 mL). t (h) is the time for ammonia production. A (cm²) is the photoelectrode's working area. n is the number of electrons transferred (n = 8 for nitrate reduction to ammonia), and F = 96500 C mol⁻¹ is the Faraday constant. M (g/mol) is the relative molecular mass of products. Q (C) is the total quantity of applied electricity.

The detection of hydrazine was carried out as followed. After the PEC reaction for 0.5 h, 2 mL electrolyte was mixed with 2 mL chromogenic

agent and put in the dark for 20 min. The chromogenic agent consists of 4 g 4-(Dimethylamino) benzaldehyde, 20 mL concentrated sulfuric acid and 200 mL anhydrous ethanol. The absorption at 460 nm was measured by an ultraviolet-visible (UV-Vis) spectrophotometer. The concentration-absorbance curve was calibrated and shown in Fig. S15.

The Griess test was adopted to evaluate the concentration of nitrite in the electrolytes. The preparation process for Griess reagents is as follows: First, 0.04 g N- (1-naphthyl) ethylenediamine dihydrochloride and 0.8 g sulfonamide were added to the mixture solution of 2 mL phosphoric acid and 10 mL deionized water and achieved a complete dissolution by ultrasonic treatment for 3 min. After diluting 0.05 mL electrolyte for 100 times with deionized water, 0.1 mL chromogenic agent was added to the electrolyte and stood for 20 min. The absorbance at 540 nm was measured by an ultraviolet-visible (UV-Vis) spectrophotometer. A series of sodium nitrate solutions with different concentrations were used to determine the standard curve. The concentration-absorbance curve was calibrated and shown in Fig. S16.

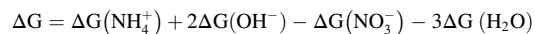
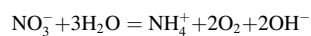
2.5. NMR measurements

To clarify the source of ammonia, the ¹⁵N isotopic labeled experiment was carried out by using the ¹⁵N isotopic K¹⁵NO₃. At the same time, the ¹⁴NH₃ was determined by the nuclear magnetic method when the reactant was K¹⁴NO₃. The concentration for nitrate reactants was 50 mM. After a photoelectrochemical reaction for 30 min, the electrolyte was diluted and the pH was adjusted to \sim 3 with 1 M HCl. Then, 0.5 mL diluted electrolyte (pH=3) was collected with a pipette, followed by the additions of 100 μ L d6-DMSO as the deuterated solvent and 50 μ L 5.0 mM DSS sodium salt solution (Sodium 3-(Trimethylsilyl)-1-propanesulfonate) as the internal standard. The presented data is the accumulated result of 256 scans on a 600 MHz NMR instrument (Bruker) equipped with an ultra-low temperature probe. First, we measured the standard curves for ¹⁵NH₃ and ¹⁴NH₃.

2.6. Efficiency of solar to ammonia (STA)

Equations for efficiency of solar to ammonia as follows:

$$STA = \left[\frac{(mmol \text{ NH}_3/\text{s}) \times 428910 \text{ J/mol}}{P_{total}(\text{mW/cm}^2) \times A(\text{cm}^2)} \right]_{AM1.5G}$$



$$\Delta G = +428.91 \text{ kJ/mol}$$

where ΔG is + 428.91 kJ/mol, (mmol NH₃/s) is ammonia production rate, mmol/s, P_{total} is incident illumination power density, 100 mW/cm² in this work, A (cm²) is illuminated electrode area, cm².

3. Results and discussion

3.1. Design, preparation and characterization of Si-based photocathode

The step-by-step fabrication process of hierarchical Si-based photocathodes is schematically illustrated in (Fig. 1a). Due to abundant reserves, suitable band structure (e.g. 1.1-eV bandgap) and non-toxicity, p-Si nanopyramids with a buried p-n junction (labeled as n⁺p-Si) were selected as the light absorber of photocathodes to harvest the photons and generate the charge carriers [35]. A thin C layer coated on the surface of n⁺p-Si (labeled as CSi, the basic characterization of C layer was shown in Fig. S1) by drop-cast method can play three important functions for Si-based photocathodes, including the protection function to afford the stable operation in the alkaline solutions [36], conductive behaviour to facilitate the transfer of photoinduced electrons [37], and

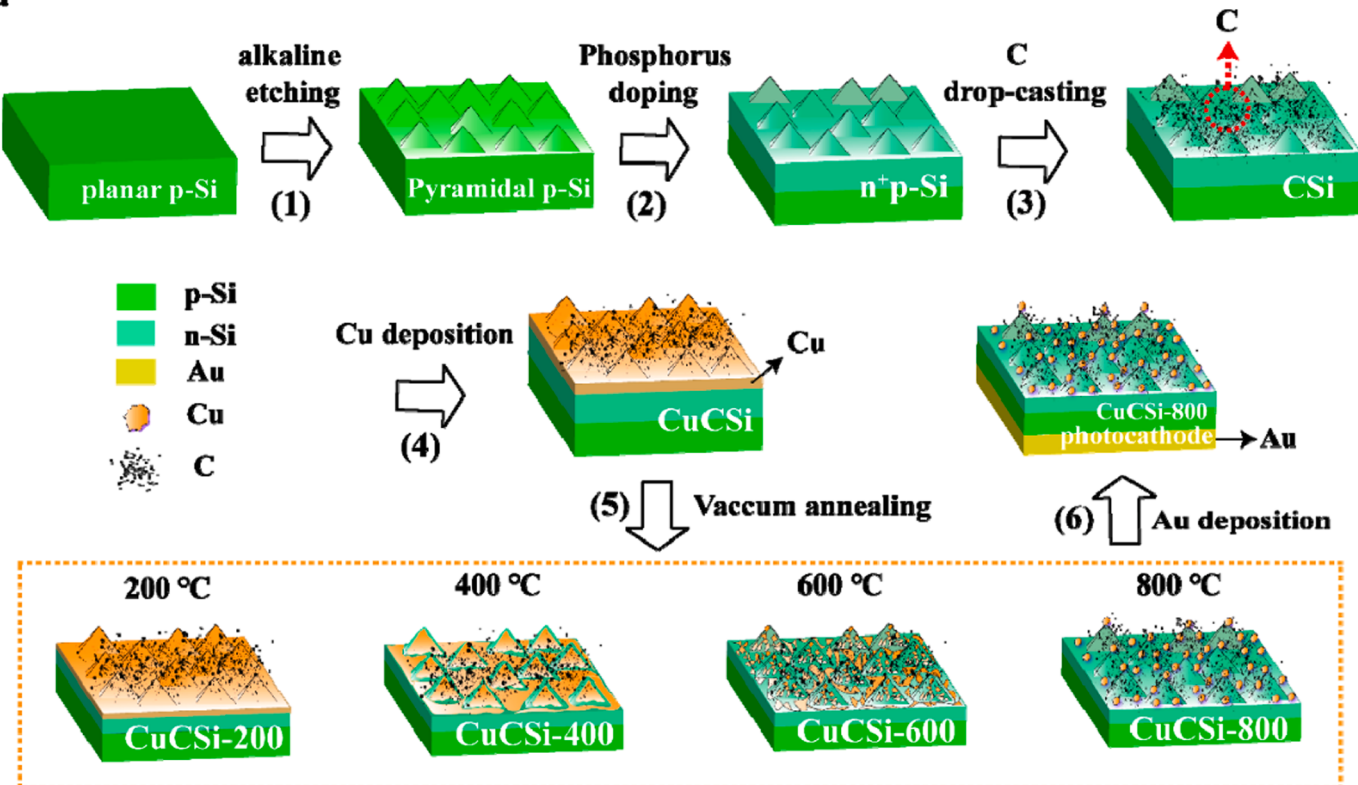
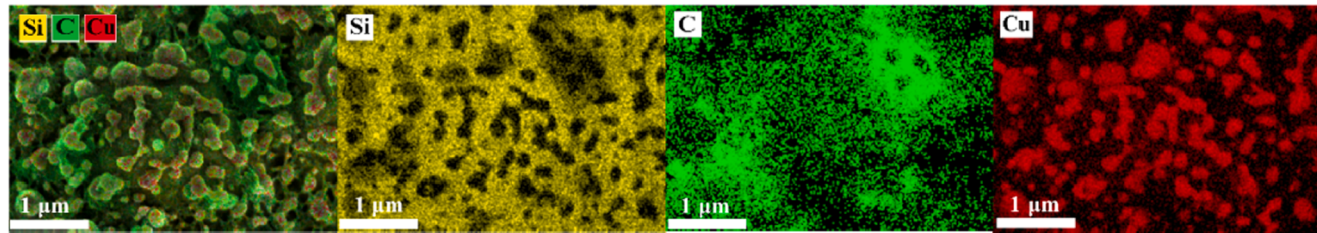
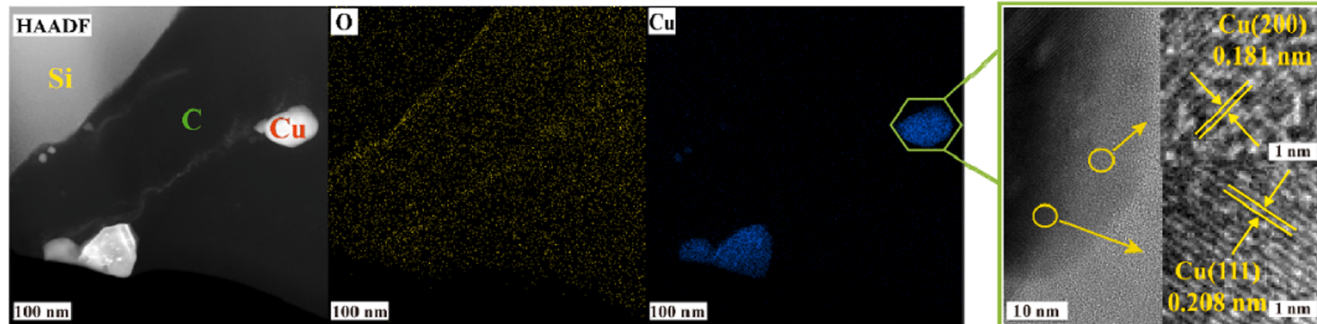
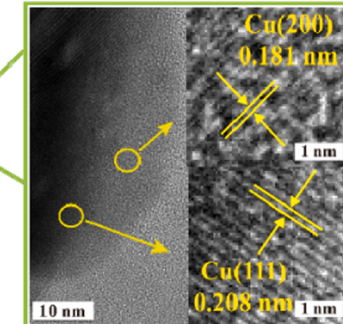
a**b****c****d**

Fig. 1. Fabrication and structural characterization of Si-based photocathodes. (a) Schematic diagram of step-by-step fabrication process of Si-based photocathodes with hierarchical structure. (b) Top view FESEM images with corresponding elemental distribution maps for CuCSI-800. (c) Cross-sectional STEM images of CuCSI-800 with O (yellow) and Cu (blue) distribution maps. d, HRTEM images of CuCSI-800 focusing on a certain Cu NP. High-magnification images on the right match the marked area.

adhesion action to anchor the Cu NPs [38]. Cu is one of the promising catalysts for NO_3RR owing to its low cost and unique electronic structure for the adsorption of electron-rich NO_3 [27]. Therefore, a metallic Cu layer with nano-sized thickness was deposited on the CSi as the cocatalyst (labeled as CuCSI), as described in Step 5 of Fig. 1a. To further optimize the PEC performance and decipher the catalytic mechanism, we minutely investigated the Cu NPs on the CSi photocathode constructed by vacuum annealing treatment of 800 °C (denoted as

CuCSI-800). In addition, the other Si-based photocathodes with different Cu NPs from different annealing treatments (denoted as CuCSI-X (200, 400 and 600)) were also prepared as the control samples (see Fig. 1a). A detailed description of the preparation method is provided in the Experimental Methods above. It should be noted that the annealing temperature no more than 800 °C hardly affects the surface morphology and properties of the n⁺p-Si wafers, in line with the application of industrialized Si-based solar cells [39].

Successful preparation of hierarchical Si-based photocathodes was confirmed by field emission scanning electron microscopy (FESEM), scanning transmission electron microscopy (STEM), and high-resolution transmission electron microscopy (HRTEM). FESEM images with energy dispersive spectroscopy (EDS) mapping indicate that the CuCSi was composed of ~ 23 nm-thickness Cu layer and ~ 7 nm-thickness C middle layer on the surface of Si nanopyramids before annealing (Fig. S2). The morphology evolution of Cu from layer to NPs were clearly observed after annealing with the increase of temperature from 200 to 800 °C (Figs. S3–4). Instead of coating the Cu layer on the surface (Fig. S2), Cu NPs with the size range from ~ 10 to 150 nm in CuCSi-800 were highly dispersed and mounted on the surface of CSi (see Fig. 1b), implying more active sites and stronger adhesion to the surface for Cu cocatalysts during PEC NO_3RR . Meanwhile, the cross-sectional microstructure of CuCSi-800 by STEM images coupled with EDS mapping (Fig. 1c and Fig. S5) also reveal the successive construction of Cu NPs and C materials on the Si surface, and some O elements seemingly surrounded the Cu NPs. HRTEM images of CuCSi-800 (Fig. 1d and Fig. S6) showed a NP with lattice spacing of ~ 0.21 and 0.18 nm, further clarifying the presence of Cu NPs with the (111) and (200) plane, in line with the characteristic diffraction peaks from X-ray diffraction (XRD, see Fig. S7). In addition, it is obviously seen that CuCSi-800 had higher peak intensity and narrower peak width than CuCSi. Finally, the optical properties and band structure of the samples were estimated by diffuse reflection spectra (Fig. S8). In comparison to the other samples, CuCSi-800 performed with a lower reflectance in the wavelength range from 350 to 800 nm, indicating the better light-harvesting ability. According to the indirect allowed transition [40,41], n^+p -Si and CSi showed the band gap of ~ 1.1 eV originated from Si, and, surprisingly, a strange bandgap of

~ 2.0 eV was found on CuCSi and CuCSi-800. According to the similar bandgap value, the occurrence of special bandgap can be attributed to the surface oxidation of Cu resulting in the formation of cuprous oxide (Cu_2O) [42] or copper oxide (CuO).

X-ray photoelectron spectroscopy (XPS) and X-ray absorption spectroscopy (XAS) were carried out to decipher the electron structure and chemical environments of the Si-based photocathodes. Different from XAS, XPS is the most surface sensitive technique from sub-nanometer to several nanometers. The full survey spectra of the surface for Si-based photocathodes presented the feature peaks of Cu 2p, C 1s, O 1s and Si 2p (Fig. S9). The atomic ratio of Si to Cu from CuCSi to CuCSi-800 was 0 and 6.68, respectively (see Fig. S10), suggesting the evolution of Cu structure from layer to NPs. In the Cu 2p spectra, the Cu NPs of CuCSi-800 consisted of Cu^0/Cu^+ and Cu^{2+} (Fig. 2a) [43], whereas Cu layer of CuCSi was composed of Cu^0/Cu^+ -dominated metallic Cu and/or Cu_2O (Fig. S11). Additionally, in the LMM Auger transition spectrum of Cu (Fig. 2b), the peaks located at 916.5 and 918.5 eV were assigned as the Cu^+ and Cu^0 in the CuCSi-800, respectively [44]. Combining the XPS data and photocathode fabrication (Fig. S8), it can be determined that the nanostructured Cu is readily oxidized in air leading to the existence of Cu^+ and Cu^{2+} , especially Cu NPs. Si 2p XPS spectra (Fig. S12) also revealed an obvious Si-O characterization peak on CuCSi-800 due to the exposure of partial Si in the ambient to form the amorphous SiO_2 [45]. To better understand the local oxidation state of Cu cocatalysts, Cu K-edge X-ray absorption near-edge structure (XANES) profiles for the Si-based photocathodes are shown in (Fig. 2c). The absorption edges of the photocathodes resided between Cu^0 (Cu foil) and Cu^+ (Cu_2O) absorption edge. Due to higher surface Gibbs free energy with more exposed surface area, Cu NPs of CuCSi-800 was easier oxidized in the air

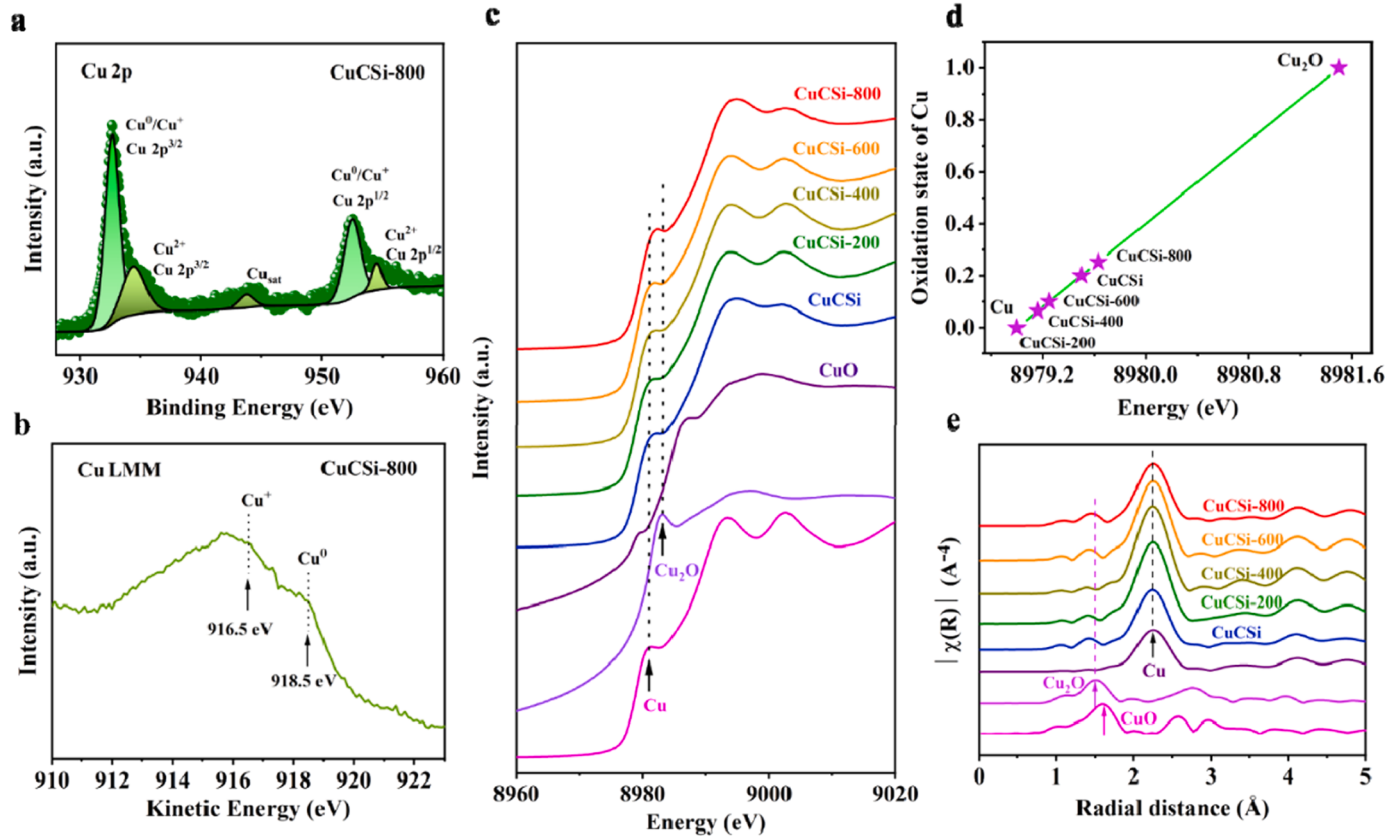


Fig. 2. XPS and XAS of the Si-based photocathodes. (a) Cu 2p spectra of XPS for CuCSi-800. The green spheres are XPS data. The black solid lines are the fitting of experimental data, which can be decomposed into a superposition of two sets of peaks. (b) Cu LMM Auger peaks with the presence of Cu^0 , Cu^+ and Cu^{2+} for CuCSi-800. (c) Cu K-edge XANES spectra of the Si-based photocathodes. The Cu foil, Cu_2O and CuO powders were employed as the references. (d) Average oxidation state of Cu in the photocathodes by Cu K-edge XANES. (e) Fourier transform (FT) k^3 -weighted extended X-ray absorption fine structure (EXAFS) spectra obtained from Cu K-edge absorption spectra.

with the edge position shifted to a higher energy compared with the other photocathodes. Fig. 2d gives a direct comparison of the oxidation state of Cu by the first derivative of normalized absorption intensity. The average oxidation state of Cu for CuCSi-800 was ~ 0.25 (Fig. 2d and Supplementary Table 1), almost identical with the data of XPS. Moreover, the R space data (Fig. 2e) that the dominant peak of CuCSi-800 is metallic Cu with a small peak at the position close to the Cu-O bond distance, which further implies the local electronic structure of Cu NPs (namely, Cu⁺-containing Cu NPs) on the CuCSi-800. However, it is difficult to find the Cu²⁺ characteristic signal in XAS spectra (Figs. 2c and 2e), which can be attributed to the micrometer depth resolution of XAS technique. On the other hand, by correlating the XPS data, XAS results and HRTEM images, we can imagine that the detected Cu²⁺ via XPS is only concentrated on the surface of Cu NPs with around one-atom thick, leading to the lack of Cu²⁺ signal in XAS spectra.

3.2. PEC NO₃RR of Si-based photocathodes in a three-electrode system

PEC NO₃RR measurements of Si-based photocathodes were first evaluated in 1M potassium hydroxide (KOH)– 0.05 M potassium nitrate (KNO₃) aqueous solution (pH = 13.8) under ambient conditions by a gas-tight two-compartment reaction cell with a three-electrode system. To accurately analyze the products of PEC NO₃RR, the indophenol blue method uniting with nuclear magnetic technology was adopted to determine the NH₃ production qualitatively and quantitatively, and the other intermediate products like nitrite (NO₂) and hydrazine (N₂H₄) were detected by the Griess test and the method of Watt and Chrissp, respectively (details described in SI)[46]. A number of standard ammonium chloride (NH₄Cl), N₂H₄ and sodium nitrite (NaNO₂) solutions with known concentrations in the electrolyte were plotted the calibration curves for all the methods (see Fig. S13–16). During PEC NO₃RR, there was no N₂H₄ product in the post-electrolysis electrolytes. Before systematically appraising the PEC NO₃RR performance of the photocathodes, five necessary control experiments were carried out to

exclude the interference of NH₃ contamination and corroborate the authenticity of PEC NO₃RR performance as below: (i) As the NO₃⁻ was added in the KOH electrolyte, there was a more prominent reduction current at lower applied potential for all the Si-based photocathodes (Fig. 3a and Fig. S17), meaning that the photocathodes have a better activity on NO₃RR than hydrogen evolution reaction (HER); (ii) Little NH₃ production was found in the experiments that took place in the dark or tested under the open-circuit voltage (Fig. S18). This preliminary result corroborates that the NH₃ is synthesized by PEC NO₃RR; (iii) The NO₃RR behaviours were controlled by the surface Cu cocatalysts and n⁺p-Si absorbers (Fig. S17 and 19), further showing that the effectiveness of Si-based photocathodes on the conversion of NO₃⁻ to NH₃; (iv) ¹⁵NO₃⁻ isotope experiments were implemented to illustrate that the nitrogen source of NH₃ was originated from the NO₃RR, because no triple peak of ¹⁴NH₄⁺ was observed in the electrolyte after photoelectrolysis (Fig. S20a); (v) The values of NH₃ concentration in the electrolyte were nearly identical using the indophenol blue method and nuclear magnetic technology (Fig. S20), demonstrating the reliability of detection method.

After affirming the true results of NO₃-to-NH₃ conversion, PEC NO₃RR performance of the photocathodes were evaluated in a three-electrode system. The NH₃ yield rate and FE of CuCSi and CuCSi-800 at each given potential in a 0.5-h period are shown in Fig. 3b. The NH₃ yield rate with relatively fixed FE (77.0–73.6%) increased from 22.9 to 47.9 $\mu\text{mol}\cdot\text{h}^{-1}\cdot\text{cm}^{-2}$ on CuCSi in the range from -0.2 to -0.8 V vs. RHE. Surprisingly, after annealing treatment of 800 °C, the NH₃ yield rate with FE of over 80% was increased markedly on CuCSi-800 by almost 2.2 times in the potential region from -0.4 to -0.8 V vs. RHE. In Fig. 3b, CuCSi-800 achieved a maximum NH₃ yield rate of 115.3 $\mu\text{mol}\cdot\text{h}^{-1}\cdot\text{cm}^{-2}$ with high FE (88.8%) at -0.6 V vs. RHE. However, CuCSi-800 at -0.2 V vs. RHE showed a worse PEC NO₃RR performance with lower NH₃ yield rate and FE than CuCSi. In fact, the linear sweep density (LSV) curves of the CuCSi-800 and CuCSi also reflects the weird phenomenon on their photocurrent density (J) as the potential is more

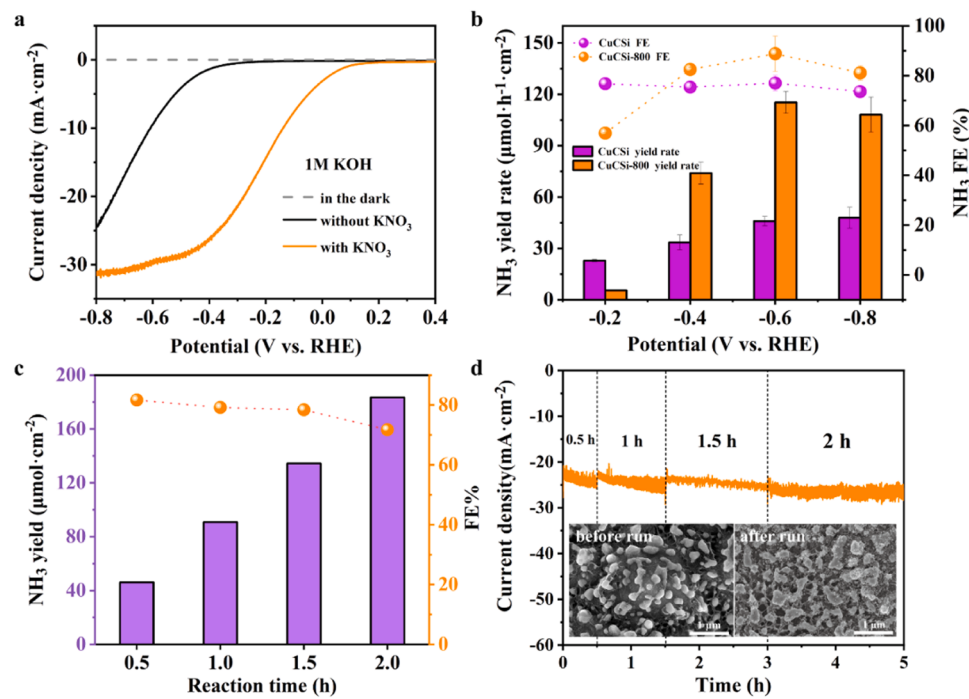


Fig. 3. PEC NO₃RR of the Si-based photocathodes in a three-electrode system. (a) Photocurrent density-potential curves of CuCSi-800 in 1 M KOH with and without 0.05 M KNO₃ under 1 sun illumination. The current density measured in dark is almost horizontal line, namely $0 \text{ mA}\cdot\text{cm}^{-2}$. (b) Yield rate of NH₃ (purple column diagrams) and FE (orange point plots) of CuCSi (purple) and CuCSi-800 (orange) at each given potential for 0.5 h. (c) Time dependence of NH₃ yield (purple column diagrams) and FE (orange point plots) obtained from CuCSi-800. (d) Photocurrent density-time plot of CuCSi-800 held at -0.6 V vs. RHE in 1 M KOH-0.05 M KNO₃. The bottom insets are the top view images of CuCSi-800 before (left) and after (right) 2-h PEC NO₃RR.

positive than -0.2 V vs. RHE (Fig. S17c). Further, the data of electrochemical impedance spectroscopy (EIS, Fig. S21) demonstrated that CuCSi-800 possesses higher and lower charge-transfer resistance at the given potential of 0 and -0.4 V vs. RHE during PEC NO_3RR , respectively, suggesting that the presence of thin dielectric SiO_2 layer on the surface of CuCSi-800 can block the transport of photoinduced electrons at low applied potentials. Additionally, EIS data of CuCSi-800 before and after 30-min PEC NO_3RR (see Fig. S21c and d) also demonstrate a good PEC stability. Meanwhile, the annealing dependence of NH_3 yield rate and FE was observed in the other photocathodes at -0.6 V vs. RHE (Fig. S22). In addition, as shown in (Fig. S23), a handful of NO_2 products were detected in the post-electrolysis electrolytes, and the NO_2 yield rate and corresponding FE were gradually decreased on CuCSi-800 with the increase of applied potentials as well as the good behaviour of PEC NO_3 -to- NH_3 conversion. To further determine the role of NO_2 products in the PEC NO_3RR process, the isotopic tracer method combining with the PEC measurements was employed to investigate the reduction of $^{14}\text{NO}_2$ and $^{15}\text{NO}_3$ on the CuCSi-800 in the pure K^{14}NO_2 and $\text{K}^{14}\text{NO}_2\text{-K}^{15}\text{NO}_3$ aqueous solution (see Fig. S24 and S25). In pure PEC NO_2 reduction reaction, CuCSi-800 showed a nearly 100% FE with a NH_3 yield rate of $115.7 \mu\text{mol}\cdot\text{h}^{-1}\cdot\text{cm}^{-2}$. Although a total FE of $\sim 100\%$ was also obtain in the $\text{K}^{14}\text{NO}_2\text{-K}^{15}\text{NO}_3$ solution, the CuCSi-800 simultaneously achieved the NO_2 reduction reaction with $\sim 80\%$ FE and $111.5 \mu\text{mol}\cdot\text{h}^{-1}\cdot\text{cm}^{-2}$ NH_3 yield rate and NO_3RR with $\sim 20\%$ FE and $28.8 \mu\text{mol}\cdot\text{h}^{-1}\cdot\text{cm}^{-2}$ NH_3 yield rate (Fig. S25a-c). On basis of these results, it can be inferred that the reduction rate of NO_2 to NH_3 is faster than that of NO_3RR , and the NO_3RR and the reduction of NO_2 to NH_3 is competitive on the surface of CuCSi-800 with different active sites. In a word, the discovered NO_2 is the by-product of PEC NO_3RR , and not the necessary intermediated product in the process.

The stability of the Si-based photocathodes is an important indicator for applying the PEC NO_3RR . As shown in (Fig. 3c), there was a linear increase in NH_3 production with slightly fluctuant FE value (over 70%) on CuCSi-800 in a 2-h PEC period, implying that the NH_3 is stably synthesized. A high NH_3 production of $183.5 \mu\text{mol}\cdot\text{cm}^{-2}$ was obtained on CuCSi-800 at 2 h. Furthermore, compared with the other photocathodes (Fig. S26a-b), CuCSi-800 showed little photocurrent decay at various given potentials for PEC NO_3RR from 0.5 to 2 h (Fig. 3d and Fig. S26c). Additionally, the Si with nano-pyramidal surface remained a high coverage of Cu-based NPs after 2-h PEC operation in alkaline solution ($\text{pH} = 13.8$, see the inset in Fig. 3d). After a 0.5-h measurement of PEC NO_3RR , the Cu concentration in the electrolyte ($1 \text{ M KOH-0.05 M KNO}_3$) was estimated by inductively coupled plasma optical emission spectrometer (ICP-OES). The results of ICP-OES (Fig. S27a) demonstrated that Cu NPs on the surface of CuCSi-800 is more stable with lower dissolution rate ($\sim 0.05 \text{ mg}\cdot\text{cm}^{-2}\cdot\text{L}^{-1}$ at 0.5 h) than Cu layer on the surface of CuCSi ($\sim 0.87 \text{ mg}\cdot\text{cm}^{-2}\cdot\text{L}^{-1}$ at 0.5 h), being ascribed to the Cu NPs mounted on the surface (Fig. 1b). However, the total loss of Cu NPs, the exfoliation corrosion of C layer, and the photooxidation of Si substrate (Fig. S27) were observed on the surface of CuCSi-800 after 10-h photoelectrolysis, meaning that the failure of the photocathode in the PEC NO_3RR . In short, the Cu NPs/C layer/Si-based photocathodes simultaneously present an outstanding PEC NO_3RR performance and an acceptable stability in the three-electrode system.

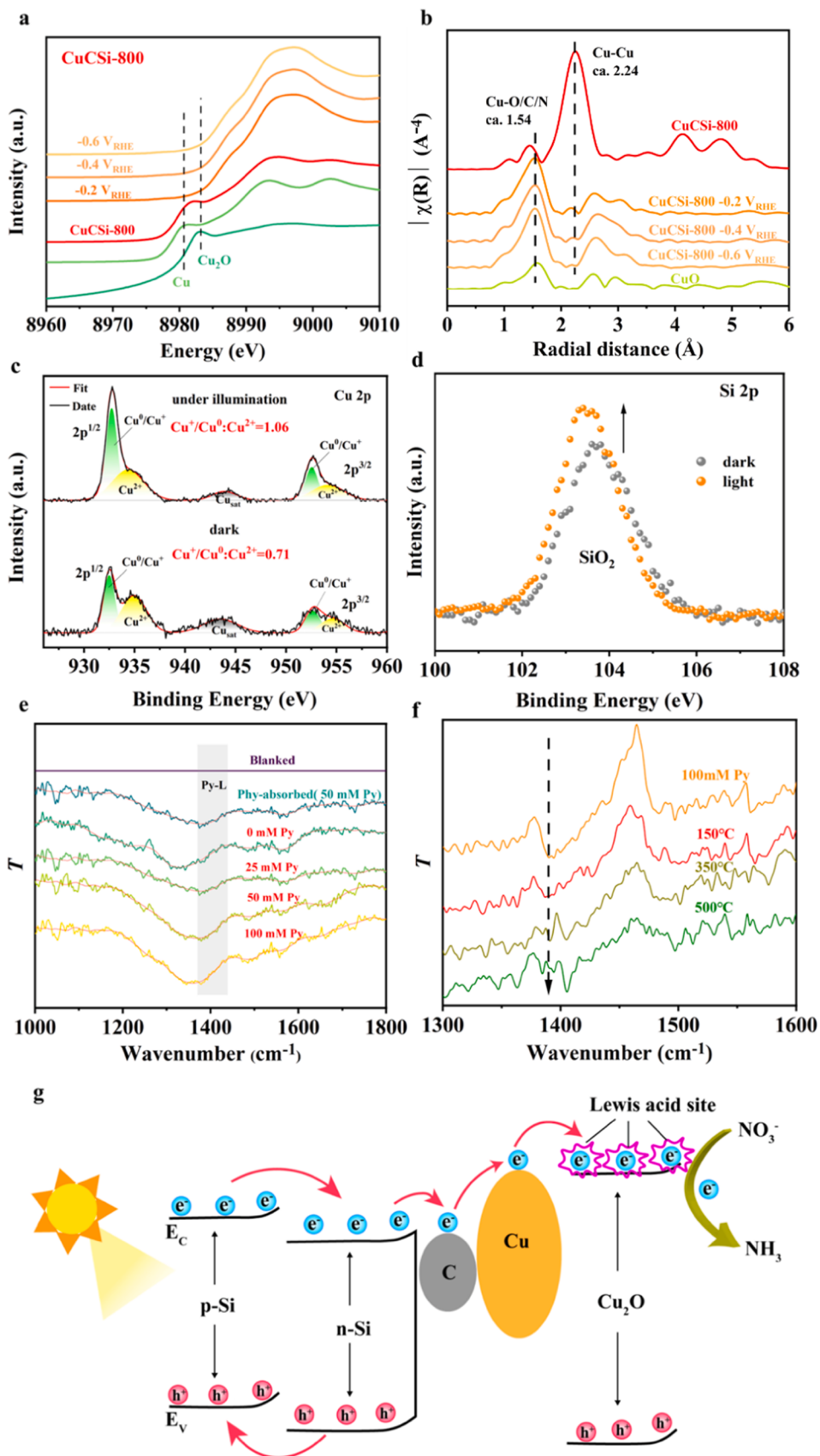
3.3. Identification of active sites for PEC NO_3RR

Quasi in-situ XAS can gather the information about the change of chemical bonds and electronic states for the Cu cocatalysts before and after NO_3RR . The Cu K-edge XANES spectra of CuCSi-800 after electrolysis were in close proximity to the spectrum of $\text{Cu}(\text{NO}_3)_2$ [47] or CuO and evidently different from that of Cu foil and Cu_2O (see Fig. 4a), in agreement with the data of operando Raman spectroscopy (Fig. S28). Cu NPs of CuCSi-800 subjected to different applied potentials from -0.2 to -0.6 V vs. RHE showed similar XANES spectra, demonstrating that the variation of chemical environments for Cu NPs is independent of the

applied potentials in given potential range during NO_3RR . Fig. 4b exhibits the R space data of CuCSi-800 before and after electrolysis to explore the precise coordination structure. In comparison to the fresh sample, CuCSi-800 after reaction owned a dominant peak centered at $\sim 1.5 \text{ \AA}$, corresponding to the Cu-X bonds (X = N or O). Integrating the abovementioned results and PEC NO_3RR measurements, it can be inferred that $\text{Cu}^+/\text{Cu}^{2+}$ -containing Cu NPs serve as reaction sites to favour the absorption and hydrogenation of NO_3^- during NO_3^- -to- NH_3 conversion.

To further uncover the reason of $\text{Cu}^+/\text{Cu}^{2+}$ -containing Cu NPs as reaction sites, operando XPS with controllable illumination conditions was employed to investigate the link between charge carriers and electronic state of CuCSi-800. The high-resolution Cu 2p spectra of CuCSi-800 (Fig. 4c) showed an unambiguous increase in the ratio of Cu^0/Cu^+ to Cu^{2+} ($\Delta R = 0.35$) during illumination relative to that before illumination (1.06), indicating the reduction of Cu^{2+} or Cu^+ . On the other hand, regarding the Si 2p spectra of CuCSi-800 (Fig. 4d), the illumination led to the increase in the intensity of Si-O peak as well as the increase of Si-O bonds. These results can be attributed to the photogenerated electrons injecting into the $\text{Cu}^+/\text{Cu}^{2+}$ sites of Cu NPs, leading to the formation of active charged sites with the reconstruction of electronic coordination environment [48]. Meanwhile, the photo-generated holes are blocked in the SiO_2 layer and beneficial to the separation of photogenerated charge carriers. In this case, $\text{Cu}^+/\text{Cu}^{2+}$ -containing Cu NPs can play an important role for storing the photoinduced electrons and yielding the Lewis acid sites (LAS), which links the NO_3^- and provides the electrons to accelerate the reaction. As well known, pyridine (Py) complexing with acid sites (e.g. LAS) on a solid surface can be easily discriminated in FT infrared spectra (FTIR) [49]. Fig. 4e collects the transmittance information of FTIR for $\text{Cu}^+/\text{Cu}^{2+}$ -containing Cu NPs with Py in various conditions after subtracting the background spectrum of Cu NPs. One wide peak at $\sim 1380 \text{ cm}^{-1}$ arising from the characteristic coordination of Py on LAS was observed in the simply physisorbed process and NO_3RR with different Py concentrations. During NO_3RR , the intensity of the characteristic peak increased with the increase of Py concentration in the electrolytes (Fig. 4e), reflecting plentiful LAS on the $\text{Cu}^+/\text{Cu}^{2+}$ -containing Cu NPs. In addition, to eliminate the interference of physisorbed Py species, the effect of annealing temperature on the intensity of the IR peaks for $\text{Cu}^+/\text{Cu}^{2+}$ -containing Cu NPs reacted in the NO_3^- -Py electrolytes is shown in Fig. 4f. When the temperature was typically performed at 150°C to remove the physisorbed Py, there was still the characteristic IR peak on the post-electrolysis Cu NPs. Over 500°C , the IR peak completely disappeared, indicating the removal of chemisorbed Py species. Consequently, the $\text{Cu}^+/\text{Cu}^{2+}$ -containing Cu NPs during NO_3RR process had the rich LAS for NO_3^- chemisorption and hydrogenation.

According to the systematic investigation and results, the work mechanism of PEC NO_3RR on the Cu NPs/C/n⁺p-Si photocathode is illustrated in (Fig. 4g). Under illumination, Si nanopyramids absorbs the incident photons to yield the electron-hole pairs. The minority carriers (electrons) are driven by built-in electric field of n⁺p heterojunction and move towards the surface of photocathode. The conductive C middle layer with suitable work function can provide effectively electron transport channels, which allow the photogenerated electrons to pass through and inject into the $\text{Cu}^+/\text{Cu}^{2+}$ -containing Cu NPs. The accepted electrons in the $\text{Cu}^+/\text{Cu}^{2+}$ -containing Cu NPs are firstly inclined to concentrate on the positive Cu sites to form the active *Cu as the reduction sites/LAS for PEC NO_3RR . When the NO_3^- species reach the *Cu, NO_3^- is adsorbed and activated to directly react with the three protons and produce the NH_3 via the participation of eight electrons from *Cu. However, a small number of NO_3^- species can connect on the other reduction sites and give rise to the existence of NO_2 in the post-electrolysis electrolytes. In a word, the formation of LAS from electron localization structure accepting electrons can provide efficient sites to revitalize the NO_3^- and protons.



(caption on next page)

Fig. 4. Analysis of active sites and proposed reaction mechanism. (a) Cu-K edge XANES spectra of CuCSi-800 before and after PEC NO_3RR at each given potential. (b) Fourier transform of the experimental EXAFS spectra of CuCSi-800 before and after PEC NO_3RR . (c) Cu 2p XPS spectra of CuCSi-800 before and during illumination. (d) Si 2p XPS spectra of CuCSi-800 before and during illumination. (e) Difference FTIR spectra of the Py region following Py adsorption at room temperature collected on Cu NPs with Py in various PEC conditions. Cu NPs was immersed into the 50 mM NO_3 -50 mM Py solution to finish the physical adsorption of Py. (f) FTIR spectra of the Py region following Py desorption at various temperature collected on Cu NPs by NO_3RR with 1 M KOH-50 mM NO_3 -100 mM Py solution. (g) Schematic representation of the work mechanism for PEC NO_3RR on the CuCSi-800.

3.4. Unbiased PEC device for efficient solar-to-ammonia conversion

Bulky TiO_2 photoanodes with the thickness of over 1.0 μm were deposited on Ti-coating quartz glass by magnetron sputtering technology (see Experimental methods above). SEM with corresponding EDS mapping, XRD patterns, and optical measurements confirmed the successful preparation of high-quality TiO_2 photoanodes (Fig. S29-31). As reported in our previous work [50], the micro-scale TiO_2 photoanode with a typical anatase phase structure with dense microstructure had a high compressive stress in the preparation process via the bombardment of high energy plasma and the absence of annealing treatment. The simple TiO_2 photoanode without any protection layer and cocatalysts presented an average saturated photocurrent density of $0.286 \pm 0.002 \text{ mA}\cdot\text{cm}^{-2}$ at 0.4 vs. RHE at 10-h PEC operation, and an early-onset potential of $\sim 0 \text{ V}$ vs. RHE for water oxidation in a three-electrode system (Fig. S32 and S33), comparing favourably among the most reported examples of dense TiO_2 photoanodes [51–53]. Considering the photocurrent density and onset potential of CuCSi-800 photocathode (Fig. 3a), the difference in active areas (A) between

photoanode and photocathode was controlled in $\sim 6.3: 1.0$ to further improve the photocurrent matching (see Fig. 5a). These very early onsets and enhanced photocurrent via the matched band structure can make the photoanode-photocathode tandem device compatible with NO_3RR and oxygen evolution reaction (OER).

Wired PEC devices for NO_3RR and OER in two-electrode system were assembled by attaching CuCSi-800 photocathodes to the quartz glass and surrounding with TiO_2 photoanodes (CuCSi-800| TiO_2 , see Fig. 5b and Fig. S34a). In this quasi-tandem design, the photoanode and photocathode lay in one plane, which can reduce the interfacial resistance and facilitate the mass and charge transfer. Under 1 sun light irradiation, the wired PEC devices showed over 2 mA photocurrent at applied bias voltage of 0 V (see Fig. S35), which is higher than cross photocurrent of single CuCSi-800 photocathode and TiO_2 photoanode in a three-electrode system needing the use of proton membrane and reference electrode (Fig. 5a). Such high photocurrent can primarily derive from the low resistance, fast mass/charge transfer and overlapped built-in electric field, leading to the shift of cross photocurrent towards the saturated photocurrent of TiO_2 photoanode. Based on the excellent

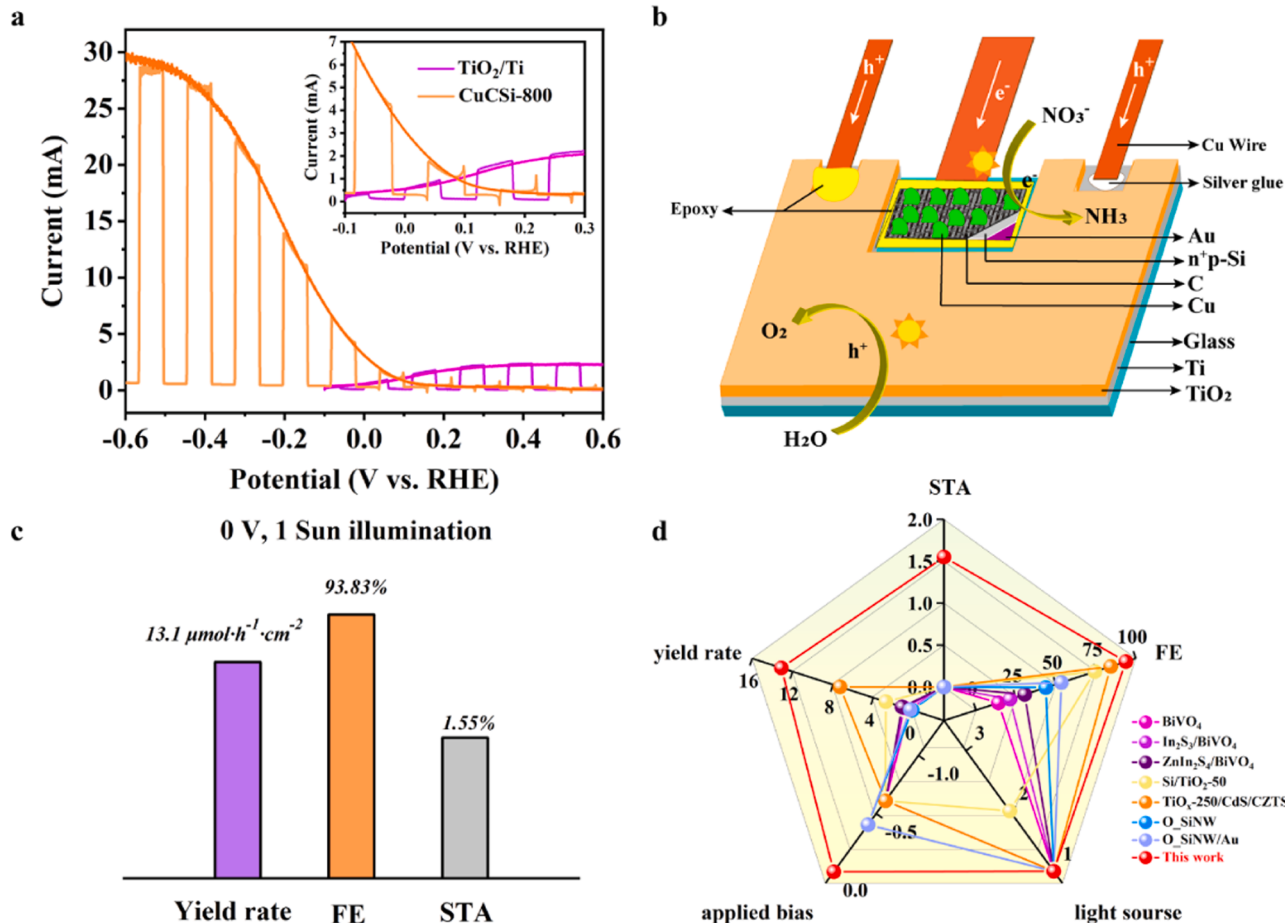


Fig. 5. Unbiased PEC device and corresponding PEC NO_3RR performance. (a) LSV curves of individual CuCSi-800 photocathode (area of 1.0 cm^2) and TiO_2 photoanode (area of $\sim 6.3 \text{ cm}^2$) in a three-electrode system. The photocurrent sign of the photocathode is inverted to emphasize photocurrent overlap. (b) Schematic depiction of the coplanar CuCSi-800| TiO_2 tandem device and their corresponding PEC reactions. (c) Performance of PEC NO_3RR on unbiased tandem device, including NH_3 yield rate, FE and STA. (d) Radar chart visualizing data on PEC NO_3RR including light source, applied bias, NH_3 yield rate, FE and STA for the previous and current work. Most PEC systems need to apply a bias voltage to compensate the insufficient photovoltage and show the limited rate and efficiency.

PEC performance, the coplanar CuCSi-800|TiO₂ tandem device realized a high NH₃ yield rate of 13.1 $\mu\text{mol}\cdot\text{h}^{-1}\cdot\text{cm}^{-2}$, an outstanding FE of 93.8% and a record solar-to-ammonia (STA) efficiency of 1.55% with respect to the area of photocathode in 10-min PEC NO₃RR at zero applied bias (Fig. 5c). The visible O₂ bubbles were also observed on the surface of TiO₂ photoanode during operation (Fig. S34d).

The PEC NO₃RR performance of our unbiased PEC devices was comparable to or even surpassed those of challenging PEC and photocatalytic NO₃RR (see Fig. 5d and additional references in Supplementary Table 2) [31,34,54,55]. Up to now, there was no reference reported in the unbiased PEC device for NO₃RR. Therefore, this comparison of performance against yield rate and FE was extended to other solar fuel technologies, for example the single photocathodes with applied potentials and photocatalysts with sacrificial reagents. Fig. 5d clearly indicates that the coplanar CuCSi-800|TiO₂ tandem device has the highest activities and efficiencies for solar-driven NO₃-to-NH₃ conversion among all the PEC NO₃RR. More broadly, this tandem device can be improved and become more suitable candidates for applications at NO₃RR and other PEC reactions, such as CO₂ reduction and biomass reaction.

4. Conclusion

We report a free-bias photoelectrochemical device for efficient solar ammonia production from NO₃ reduction reaction. This device integrating a hierarchical-structured Si-based photocathode and micro-scale TiO₂ photoanode attain a record solar-to-ammonia efficiency of 1.55%, surmounting the current solar-driven ammonia synthesis technologies. In a three-electrode system, the Si-based photocathode with Cu⁺/Cu²⁺-containing Cu nanoparticles affords an excellent NH₃ yield rate of 115.3 $\mu\text{mol}\cdot\text{h}^{-1}\cdot\text{cm}^{-2}$ and faradaic efficiency of 88.8% at -0.6 V vs. RHE. On basis of the advanced analysis, the Lewis acid sites formed on the Cu⁺/Cu²⁺-containing Cu nanoparticles can promote the adsorption and hydrogenation of NO₃ for NH₃ production. The proof-of-concept unbiased device and efficient photocathode help envision a future in which artificial nitrogen cycle may access the vast potential of solar, water and oxynitride pollution gas (e.g. NO₂).

CRediT authorship contribution statement

Ding Jingjing: Writing – original draft, Methodology. **Jiang San Ping:** Writing – review & editing. **Wang Shuangyin:** Writing – review & editing. **Zhang Xiaoran:** Methodology. **zheng jianyun:** Writing – review & editing, Writing – original draft, Supervision, Conceptualization. **Johannessen Bernt:** Methodology. **Lyu Yanhong:** Writing – original draft, Methodology. **Zhou Huaijuan:** Writing – review & editing, Methodology.

Declaration of Competing Interest

The authors declare no competing interests.

Data availability

Data will be made available on request.

Acknowledgements

The authors are grateful to the National Natural Science Foundation of China (22075075), the Key R&D Program of China (2021YFA1500900 and 2020YFA0710000), the Outstanding Youth Scientist Foundation of Hunan Province (2022JJ10023), the Hunan Province of Huxiang Talent project (2021RC3051), the Provincial Natural Science Foundation of Guangdong (2023A1515011745), the Provincial Natural Science Foundation of Hunan (2021JJ40140), and the Research Foundation of Education Bureau of Hunan Province (21B0812)

for financial support of this research.

Appendix A. Supporting information

Supplementary data associated with this article can be found in the online version at doi:10.1016/j.apcatb.2024.123735.

References

- R.F. Service, New recipe produces ammonia from air, water, and sunlight, -610, Science 345 (2014) 610, <https://doi.org/10.1126/science.345.6197.610>.
- I. Coric, B.Q. Mercado, E. Bill, D.J. Vinyard, P.L. Holland, Binding of dinitrogen to an iron-sulfur-carbon site, Nature 526 (2015) 96–99, <https://doi.org/10.1038/nature15246>.
- K.M. Lancaster, M. Roemelt, P. Ettenhuber, Y.L. Hu, M.W. Ribbe, F. Neese, U. Bergmann, S. DeBeer, X-ray emission spectroscopy evidences a central carbon in the nitrogenase iron-molybdenum cofactor, Science 334 (2011) 974–977, <https://doi.org/10.1126/science.1206445>.
- W.H. Guo, K.X. Zhang, Z.B. Liang, R.Q. Zou, Q. Xu, Electrochemical nitrogen fixation and utilization: theories, advanced catalyst materials and system design, Chem. Soc. Rev. 48 (2019) 5658–5716, <https://doi.org/10.1039/c9cs00159j>.
- J. Liu, M.S. Kelley, W.Q. Wu, A. Banerjee, A.P. Douvalis, J.S. Wu, Y.B. Zhang, G. C. Schatz, M.G. Kanatzidis, Nitrogenase-mimic iron-containing chalcogels for photochemical reduction of dinitrogen to ammonia, Proc. Natl. Acad. Sci. USA 113 (2016) 5530–5535, <https://doi.org/10.1073/pnas.1605512113>.
- Department, S.R., S, Ed. (2023). (<https://www.statista.com/statistics/1266378/global-ammonia-production/>).
- Service, R.F., LIQUID SUNSHINE, Science, 361 (2018) 120–123. (<https://www.science.org/doi/10.1126/science.361.6398.120>).
- A.M. Elbaz, S. Wang, T.F. Guiberti, W.L. Roberts, Review on the recent advances on ammonia combustion from the fundamentals to the applications, Fuel Commun. 10 (2022), <https://doi.org/10.1016/j.jfueco.2022.100053>.
- Y.M. Li, Y.K. Go, H. Ooka, D.P. He, F.M. Jin, S.H. Kim, R. Nakamura, Enzyme mimetic active intermediates for nitrate reduction in neutral aqueous media, Angew. Chem. -Int. Ed. 59 (2020) 9744–9750, <https://doi.org/10.1002/anie.202002647>.
- J. Li, G.M. Zhan, J.H. Yang, F.J. Quan, C.L. Mao, Y. Liu, B. Wang, F.C. Lei, L.J. Li, A. W.M. Chan, et al., Efficient ammonia electrosynthesis from nitrate on strained ruthenium nanoclusters, J. Am. Chem. Soc. 142 (2020) 7036–7046, <https://doi.org/10.1021/jacs.0c00418>.
- J. Zhang, W.H. He, T. Quast, J.R.C. Junqueira, S. Saddeler, S. Schulz, W. Schuhmann, Single-entity electrochemistry unveils dynamic transformation during tandem catalysis of Cu₂O and Co₃O₄ for converting NO₃- to NH₃, Angew. Chem. -Int. Ed. 9 (2023), <https://doi.org/10.1002/anie.202214830>.
- H. Xu, Y.Y. Ma, J. Chen, W.X. Zhang, J.Y. Yang, Electrocatalytic reduction of nitrate - a step towards a sustainable nitrogen cycle, Chem. Soc. Rev. 51 (2022) 2710–2758, <https://doi.org/10.1039/d1cs00857a>.
- Y.T. Wang, Y.F. Yu, R.R. Jia, C. Zhang, B. Zhang, Electrochemical synthesis of nitric acid from air and ammonia through waste utilization, Natl. Sci. Rev. 6 (2019) 730–738, <https://doi.org/10.1093/nsr/nwz019>.
- Y.T. Wang, C.H. Wang, M.Y. Li, Y.F. Yu, B. Zhang, Nitrate electroreduction: mechanism insight, in situ characterization, performance evaluation, and challenges, Chem. Soc. Rev. 50 (2021) 6720–6733, <https://doi.org/10.1039/dics00116g>.
- L.Z. Sun, B. Liu, Mesoporous PdN alloy nanocubes for efficient electrochemical nitrate reduction to ammonia, Adv. Mater. 35 (2023) 2207305, <https://doi.org/10.1002/adma.202207305>.
- L.Z. Sun, H.Q. Yao, F.R. Jia, B. Liu, Intermediate confinement for selective ammonia electrosynthesis from nitrate on robust mesoporous metal catalysts, Adv. Energy Mater. 13 (2023) 2302274, <https://doi.org/10.1002/aenm.202302274>.
- L.Z. Sun, H.Q. Yao, Y.Z. Wang, C.B. Zheng, B. Liu, Mesostructures engineering to promote selective nitrate-to-ammonia electroreduction, Adv. Energy Mater. 13 (2023) 2303054, <https://doi.org/10.1002/aenm.202303054>.
- X.W. Min, B. Liu, Microenvironment engineering to promote selective ammonia electrosynthesis from nitrate over a PdCu hollow catalyst, Small 19 (2023) 2300794, <https://doi.org/10.1002/smll.202300794>.
- Y.H. Wang, A. Xu, Z.Y. Wang, L.S. Huang, J. Li, F.W. Li, J. Wicks, M.C. Luo, D. H. Nam, C.S. Tan, et al., Enhanced nitrate-to-ammonia activity on copper-nickel alloys via tuning of intermediate adsorption, J. Am. Chem. Soc. 142 (2020) 5702–5708, <https://doi.org/10.1021/jacs.9b13347>.
- S.E. Bae, K.L. Stewart, A.A. Gewirth, Nitrate adsorption and reduction on Cu(100) in acidic solution, J. Am. Chem. Soc. 129 (2007) 10171–10180, <https://doi.org/10.1021/ja071330n>.
- M.S. Yang, G. Meng, H.Y. Li, T.R. Wei, Q. Liu, J. He, L.G. Feng, X.P. Sun, X.J. Liu, Bifunctional bimetallic oxide nanowires for high-efficiency electrosynthesis of 2,5-furandicarboxylic acid and ammonia, J. Colloid Interface Sci. 652 (2023) 155–163, <https://doi.org/10.1016/j.jcis.2023.08.079>.
- G.K. Zhang, Y.Y. Wan, X.J. Liu, K. Chu, Ampere-level nitrate electroreduction to ammonia over monodispersed Bi-doped Fe₂S₂, ACS Nano 17 (2023) 21328–21336, <https://doi.org/10.1021/acsnano.3c05946>.
- S.S. Chen, G.C. Qi, R.L. Yin, Q. Liu, L.G. Feng, X.C. Feng, G.Z. Hu, J. Luo, X.J. Liu, W.X. Liu, Electrocatalytic nitrate-to-ammonia conversion on CoO/CuO nanoarrays

using Zn-nitrate batteries, *Nanoscale* (48) (2023) 19577–19585, <https://doi.org/10.1039/D3NR05254K>.

[24] G.F. Chen, Y.F. Yuan, H.F. Jiang, S.Y. Ren, L.X. Ding, L. Ma, T.P. Wu, J. Lu, H. Wang, Electrochemical reduction of nitrate to ammonia via direct eight-electron transfer using a copper-molecular solid catalyst, *Nat. Energy* 5 (2020) 605–613, <https://doi.org/10.1038/s41560-020-0654-1>.

[25] Z.Y. Wu, M. Karamad, X. Yong, Q.Z. Huang, D.A. Cullen, P. Zhu, C.A. Xia, Q. F. Xiao, M. Shakouri, F.Y. Chen, et al., Electrochemical ammonia synthesis via nitrate reduction on Fe single atom catalyst, *Nat. Commun.* 12 (2021) 10, <https://doi.org/10.1038/s41467-021-23115-x>.

[26] F.Y. Chen, Z.Y. Wu, S. Gupta, D.J. Rivera, S.V. Lambeets, S. Pecaut, J.Y.T. Kim, P. Zhu, Y.Z. Finfrock, D.M. Meira, et al., Efficient conversion of low-concentration nitrate sources into ammonia on a Ru-dispersed Cu nanowire electrocatalyst, *Nat. Nanotechnol.* 17 (2022) 759, <https://doi.org/10.1038/s41565-022-01121-4>.

[27] W.H. He, J. Zhang, S. Dieckhofer, S. Varhade, A.C. Brix, A. Lielpetere, S. Seisel, J.R. C. Junqueira, W. Schuhmann, Splicing the active phases of copper/cobalt-based catalysts achieves high-rate tandem electroreduction of nitrate to ammonia, *Nat. Commun.* 13 (2022) 13, <https://doi.org/10.1038/s41467-022-28728-4>.

[28] K. Fan, W.F. Xie, J.Z. Li, Y.N. Sun, P.C. Xu, Y. Tang, Z.H. Li, M.F. Shao, Active hydrogen boosts electrochemical nitrate reduction to ammonia, *Nat. Commun.* 13 (2022) 13, <https://doi.org/10.1038/s41467-022-35664-w>.

[29] D.G. Nocera, Solar fuels and solar chemicals industry, *Acc. Chem. Res.* 50 (2017) 616–619, <https://doi.org/10.1021/acs.accounts.6b00615>.

[30] D. Antón-García, E. Edwards Moore, M.A. Bajada, A. Eisenschmidt, A.R. Oliveira, I.A.C. Pereira, J. Warnan, E. Reisner, Photoelectrochemical hybrid cell for unbiased CO₂ reduction coupled to alcohol oxidation, *Nat. Synth.* 1 (2022) 77–86, <https://doi.org/10.1038/s44160-021-00003-2>.

[31] H.E. Kim, J. Kim, E.C. Ra, H.M. Zhang, Y.J. Jang, J.S. Lee, Photoelectrochemical nitrate reduction to ammonia on ordered silicon nanowire array photocathodes, *Angew. Chem. -Int. Ed.* 61 (2022) 7, <https://doi.org/10.1002/anie.202204117>.

[32] J.Y. Zheng, L. Jiang, Y.H. Lyu, S.P. Jian, S.Y. Wang, Green synthesis of nitrogen-to-ammonia fixation: past, present, and future, *Energy Environ. Mater.* 5 (2022) 452–457, <https://doi.org/10.1002/eem2.12192>.

[33] B.H.R. Suryanto, H.L. Du, D.B. Wang, J. Chen, A.N. Simonov, D.R. MacFarlane, Challenges and prospects in the catalysis of electroreduction of nitrogen to ammonia, *Nat. Catal.* 2 (2019) 290–296, <https://doi.org/10.1038/s41929-019-0252-4>.

[34] S.J. Zhou, K.W. Sun, C.Y. Toe, J. Yin, J.L. Huang, Y.Y. Zeng, D.D. Zhang, W.J. Chen, O.F. Mohammed, X.J. Hao, et al., Engineering a Kesterite-Based Photocathode for Photoelectrochemical Ammonia Synthesis from NO_x Reduction, *Adv. Mater.* 34 (2022) 11, <https://doi.org/10.1002/adma.202201670>.

[35] M. Caban-Acevedo, M.L. Stone, J.R. Schmidt, J.G. Thomas, Q. Ding, H.C. Chang, M. L. Tsai, J.H. He, S. Jin, Efficient hydrogen evolution catalysis using ternary pyrite-type cobalt phosphosulphide, *Nat. Mater.* 14 (2015) 1245–1251, <https://doi.org/10.1038/nmat4410>.

[36] A.C. Nielander, M.J. Bierman, N. Petrone, N.C. Strandwitz, S. Ardo, F. Yang, J. Hone, N.S. Lewis, Photoelectrochemical behavior of n-type Si(111) Electrodes Coated With a Single Layer of Graphene, *J. Am. Chem. Soc.* 135 (2013) 17246–17249, <https://doi.org/10.1021/ja407462g>.

[37] R. Matheu, I.A. Moreno-Hernandez, X. Sala, H.B. Gray, B.S. Brunschwig, A. Llobet, N.S. Lewis, Photoelectrochemical behavior of a molecular Ru-based water oxidation catalyst bound to TiO₂-protected Si photoanodes, *J. Am. Chem. Soc.* 139 (2017) 11345–11348, <https://doi.org/10.1021/jacs.7b06800>.

[38] J.G. Hou, H.J. Cheng, O. Takeda, H. Zhu, Three-dimensional bimetal-graphene-semiconductor coaxial nanowire arrays to harness charge flow for the photochemical reduction of carbon dioxide, *Angew. Chem. -Int. Ed.* 54 (2015) 8480–8484, <https://doi.org/10.1002/anie.201502319>.

[39] F. Fu, J. Li, T.C.J. Yang, H. Liang, A. Faes, Q. Jeangros, C. Ballif, Y. Hou, Monolithic perovskite-silicon tandem solar cells: from the lab to fab? *Adv. Mater.* 34 (2022) <https://doi.org/10.1002/adma.202106540>.

[40] J.Y. Zheng, Y.H. Lyu, R.L. Wang, C. Xie, H.J. Zhou, S.P. Jiang, S.Y. Wang, Crystalline TiO₂ protective layer with graded oxygen defects for efficient and stable silicon-based photocathode, *Nat. Commun.* 9 (2018) 10, <https://doi.org/10.1038/s41467-018-05580-z>.

[41] J.Y. Zheng, Y.H. Lyu, C. Xie, R.L. Wang, L. Tao, H.B. Wu, H.J. Zhou, S.P. Jiang, S. Y. Wang, Defect-enhanced charge separation and transfer within protection layer/semiconductor structure of photoanodes, *Adv. Mater.* 30 (2018) 7, <https://doi.org/10.1002/adma.201801773>.

[42] L.F. Pan, J.H. Kim, M.T. Mayer, M.K. Son, A. Ummadisingu, J.S. Lee, A. Hagfeldt, J. S. Luo, M. Gratzel, Boosting the performance of Cu₂O photocathodes for unassisted solar water splitting devices, *Nat. Catal.* 1 (2018) 412–420, <https://doi.org/10.1038/s41929-018-0077-6>.

[43] X.R. Zhang, Y. Lyu, H.J. Zhou, J.Y. Zheng, A.B. Huang, J.J. Ding, C. Xie, R. De Marco, N. Tsud, V. Kalinovych, et al., Photoelectrochemical N₂-to-NH₃ Fixation with High Efficiency and Rates via Optimized Si-Based System at Positive Potential versus Li^{0/+}, *Adv. Mater.* 35 (2023) 9, <https://doi.org/10.1002/adma.2022111894>.

[44] D.F. Gao, I. Sinev, F. Scholten, R.M. Aran-Ais, N.J. Divins, K. Kvashnina, J. Timoshenko, B. Roldan Cuenya, Selective CO₂ electroreduction to ethylene and mult carbon alcohols via electrolyte-driven nanostructuring, *Angew. Chem. -Int. Ed.* 58 (2019) 17047–17053, <https://doi.org/10.1002/anie.201910155>.

[45] J.Y. Zheng, Y. Lyu, A.B. Huang, B. Johannessen, X. Cao, S.P. Jiang, S.Y. Wang, Deciphering the synergy between electron localization and alloying for photoelectrochemical nitrogen reduction to ammonia, *Chin. J. Catal.* 45 (2023) 141–151, [https://doi.org/10.1016/s1872-2067\(22\)64178-0](https://doi.org/10.1016/s1872-2067(22)64178-0).

[46] J.Y. Zheng, Y.H. Lyu, M. Qiao, R.L. Wang, Y.Y. Zhou, H. Li, C. Chen, Y.F. Li, H. J. Zhou, S.P. Jiang, et al., Photoelectrochemical synthesis of ammonia on the aerophilic-hydrophilic heterostructure with 37.8% efficiency, *Chem* 5 (2019) 617–633, <https://doi.org/10.1016/j.chempr.2018.12.003>.

[47] M. Larsson, J.B. Linden, S. Kaur, B. Le Cerf, I. Kempson, Cu K-edge XANES: polymer, organic, inorganic spectra, and experimental considerations, *Powder Diffr.* 32 (2017) S28–S32, <https://doi.org/10.1017/s0885715617000756>.

[48] J.Y. Zheng, Y.H. Lyu, M. Qiao, J.P. Veder, R.D. Marco, J. Bradley, R.L. Wang, Y. F. Li, A.B. Huang, S.P. Jiang, et al., Tuning the electron localization of gold enables the control of nitrogen-to-ammonia fixation, *Angew. Chem. -Int. Ed.* 58 (2019) 18604–18609, <https://doi.org/10.1002/anie.201909477>.

[49] S. Bordiga, C. Lamberti, F. Bonino, A. Travert, F. Thibault-Starzyk, Probing zeolites by vibrational spectroscopies, *Chem. Soc. Rev.* 44 (2015) 7262–7341, <https://doi.org/10.1039/c5cs00396b>.

[50] B.B. Wu, Y. Lyu, W. Chen, J.Y. Zheng, H.J. Zhou, R. De Marco, N. Tsud, K.C. Prince, V. Kalinovych, B. Johannessen, et al., Compression stress-induced internal magnetic field in bulky TiO₂ photoanodes for enhancing charge-carrier dynamics, *Jacs Au* 11 (2023), <https://doi.org/10.1021/jacsau.2c00690>.

[51] D.L. Jiang, H.J. Zhao, S.Q. Zhang, R. John, G.D. Will, Photoelectrochemical measurement of phthalic acid adsorption on porous TiO₂ film electrodes, *J. Photochem. Photobiol. a-Chem.* 156 (2003) 201–206, [https://doi.org/10.1016/s1010-6030\(02\)00409-4](https://doi.org/10.1016/s1010-6030(02)00409-4).

[52] C.J. Liu, L.M. Chen, X. Su, S. Chen, J. Zhang, H.P. Yang, Y. Pei, Activating a TiO₂/BiVO₄ film for photoelectrochemical water splitting by constructing a heterojunction interface with a uniform crystal plane orientation, *Acs Appl. Mater. Interfaces* 14 (2022) 2316–2325, <https://doi.org/10.1021/acsami.1c20038>.

[53] X.D. Li, C.T. Gao, H.G. Duan, B.G. Lu, X.J. Pan, E.Q. Xie, Nanocrystalline TiO₂ film based photoelectrochemical cell as self-powered UV-photodetector, *Nano Energy* 1 (2012) 640–645, <https://doi.org/10.1016/j.nanoen.2012.05.003>.

[54] M.Q. Xu, F.C. Xu, K.L. Zhu, X.D. Xu, P. Deng, W.B. Wu, W. Ye, Z.T. Sun, P. Gao, Atomic layer deposition technique refining oxygen vacancies in TiO₂ passivation layer for photoelectrochemical ammonia synthesis, *Compos. Commun.* 29 (2022) 5, <https://doi.org/10.1016/j.coco.2021.101037>.

[55] F.F. Wang, Q.J. Ding, J.R. Ding, Y.J. Bai, H.Y. Bai, W.Q. Fan, Frustrated Lewis pairs boosting photoelectrochemical nitrate reduction over ZnIn₂S₄/BiVO₄ heterostructure, *Chem. Eng. J.* 450 (2022) 10, <https://doi.org/10.1016/j.cej.2022.138260>.